Dynamics of a Miyamoto-Nagai Disk in a Hernquist Halo: Equilibrium and the Effect of Three Different Perturbers.

Ludovica Carbone 866609

Dynamics of Stellar Systems 2023/2024

Contents

1 Overview

This report focuses on the study of a Miyamoto-Nagai disk in equilibrium, embedded whitin a dark matter halo represented by a static Hernquist potential. The first part of the study is dedicated to identify the conditions required for the disk to reach a stable equilibrium state. In the second part, a perturber is introduced into the system to examine the effects of dynamical friction and how it influences the system's evolution over time. The simulation is conducted with three perturbers of varying masses to illustrate how the effects of dynamical friction depend on the perturber's mass.

2   Theoretical Background

This section provides a brief overview of the distributions used in the study. The following section discusses the conditions necessary to establish the system's equilibrium.

2.1   Miyamoto-Nagai Disk

The Miyamoto-Nagai potential, along with its corresponding density distribution, was selected to model a disk galaxy.

The potential of the Miyamoto-Nagai disk is presented below [1]:

$$\Phi(R, z) = \frac{-GM_D}{\sqrt{R^2 + \left(a + \sqrt{z^2 + b^2}\right)^2}} \tag{1}$$

where: R and z are the cylindrical coordinates, M_D is the total mass of the disk, a and b are scale parameters determining the radial and vertical structure of the disk, respectively.

The density corresponding to this potential can be computed using the Poisson equation [1]

$$\rho(R, z) = \frac{b^2 M_D}{4\pi} \frac{(aR^2 + (a + 3\sqrt{z^2 + b^2})(a + \sqrt{z^2 + b^2})^2)}{(R^2 + (a + \sqrt{z^2 + b^2})^2)^{5/2}(z^2 + b^2)^{3/2}} \tag{2}$$

The Miyamoto-Nagai disk profile reduces to the razor-thin Kuzmin disk when $b \to 0$, this potential reduces to that of a Plummer sphere when $a \to 0$ [2], a spherical density distribution. The Miyamoto-Nagai density model differs significantly from the exponential radial behavior observed in realistic galactic disks, as its density goes as R^{-3} at large radii ($R \gg a$) rather than exponentially. While this causes the density to remain too high at large radii, the model's simplicity and computational efficiency make it a popular choice, in particular because computing the gravitational potential for an exponential disk, is significantly more complex.

2.2   Hernquist Halo

To make the simulation more realistic, we embedded the disk within a static Hernquist potential, a spherical symmetric potential-density pair, which is used to represent the influence of a dark matter halo.

The Hernquist potential is given by [3]:

$$\Phi(r) = -\frac{GM_H}{r + a_H} \tag{3}$$

where M_H is the total mass of the halo, r is the radial distance from the center, and a_H is the scale radius, a parameter that defines the radial dimension of the halo.

To compute the potential exerted by the halo on a particle, we used Newton's shell theorem to account only for the mass enclosed within the particle's radial distance. The enclosed mass is given by:

$$M_H(r) = M_H \frac{r^2}{(r + a_H)^2}, \tag{4}$$

and the resulting potential becomes:

$$\Phi_{\text{halo}}(r) = \frac{-GM_H(r)}{r} = -\frac{G}{r} M_H \frac{r^2}{(r + a_H)^2}. \tag{5}$$

---

[1]The Poisson equation is given by: $\nabla^2 \Phi = 4\pi G\rho$, where Φ is the gravitational potential, G is the gravitational constant, and ρ is the mass density.

3 Initial Conditions

Simulations are performed using a treecode, which is a program designed for self-consistent N-body simulations, as described in [4]. The program operates using internal units (IU), assuming that the gravitational constant G is set to 1 IU.

We began the initialization of our simulation by selecting the mass for the Hernquist halo: $M_H = 10^{12} \, \mathrm{M_\odot}$. Using the empirical relation from [5], we computed the mass of the disk as:

$$\frac{M_{\mathrm{star}}}{M_{\mathrm{halo}}} = 2N \left[\left(\frac{M_{\mathrm{halo}}}{M_1} \right)^{-\beta} + \left(\frac{M_{\mathrm{halo}}}{M_1} \right)^{\gamma} \right]^{-1}, \tag{6}$$

where N, M_1, β, and γ are parameters with estimated values provided in the paper. From this computation, the mass of the disk was determined to be $M_D = 2.43 \cdot 10^{10} \, \mathrm{M_\odot}$.

We then rescaled the masses from solar masses to internal units (IU), resulting in $M_H = 10^3 \, \mathrm{IU}$ and $M_D = 34.28 \, \mathrm{IU}$.

The other relevant geometrical constants are set as follows:

- $a_D = 3$ IU

- $b = 0.05 \cdot \mathrm{a} = 0.15$ IU

- $a_H = 6$ IU

We simulated a total of 20001 particles, considering 20000 for the disk and one representing the perturber. The mass of a disk particle is $M_D/\mathrm{N_{part}} = 0.0017 \, \mathrm{IU}$

3.1 Disk Particles Positions

To sample the positions of the disk particles, we define the probability density as $p(r) = \frac{M(r)}{M_{\mathrm{tot}}}$. Specifically, for our case, we have an axisymmetric density that can be written in cylindrical coordinates as:

$$p(R, z) = \frac{M(R, z)}{M_{tot}} = \frac{\rho(R, z) 2\pi R dR dz}{M_{tot}}. \tag{7}$$

We implemented a Monte Carlo Markov Chain (MCMC) using the `emcee` library, designing the log likelihood function as $L = \log(\rho(R, z) 2\pi R)$, where $\rho(R, z)$ is the mass density from equation 2. We applied a uniform prior for R between 0 and 30, for z between 0 and 5, and for the angle θ between 0 and 2π. By running 30 walkers for $5 \cdot 10^4$ steps, the distribution can be sampled in around 30 seconds. From the resulting chains, we then select the desired number of points from the unique values. The resulting corner plots are shown in Figure 1.
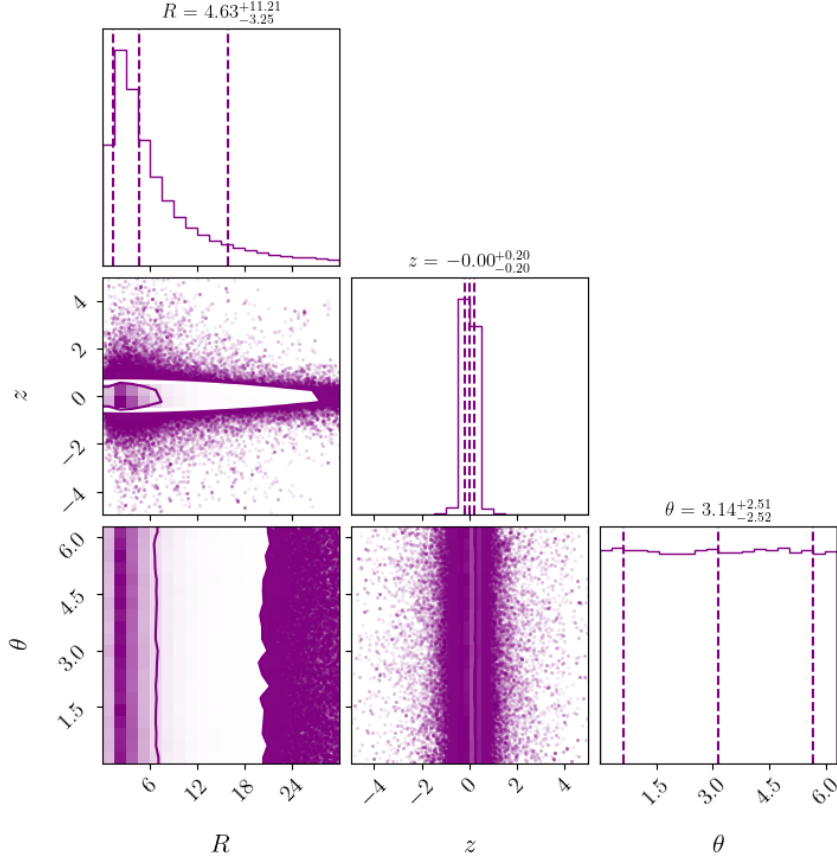
Figure 1: Corner plots of the MCMC unique samples for the R, z, θ components of a Miyamoto-Nagai disk.

To verify the consistency of the sampling with the theoretical distribution, we compare the theoretical surface density, $\Sigma(R)$, computed through numerical integration (eq. 8), with the "experimental" surface density.

The theoretical surface density is given by:

$$\Sigma(R) = 2 \int_0^{z_{\max}} \rho(R, z)\, dz \tag{8}$$

The experimental surface density is computed by binning the particles' radial distances and calculating the mass within each bin, normalized by the bin area. Errors are estimated using Poisson statistics, where the fractional error is based on the number of particles in each bin. For bins with no particles, the error is assumed to be zero. Assuming all particles have equal mass, the numerical surface density in a bin is given by:

$$\Sigma = \frac{mN}{A} \tag{9}$$

where N is the number of particles in that bin. The errors on Σ are computed using Poisson statistics and error propagation rules as:

$$\sigma_\Sigma = \frac{\partial \Sigma}{\partial N} \sigma_N = \frac{m}{A} \sqrt{N} \frac{N}{N} = \frac{\Sigma}{\sqrt{N}} \tag{10}$$

A fit is performed leaving the disk mass as a free parameter. The agreement between the theoretical and experimental distributions seems strong even if the errors are clearly underestimated. As a result, the chi-squared (χ^2) statistic does not provide a meaningful measure of goodness of fit.
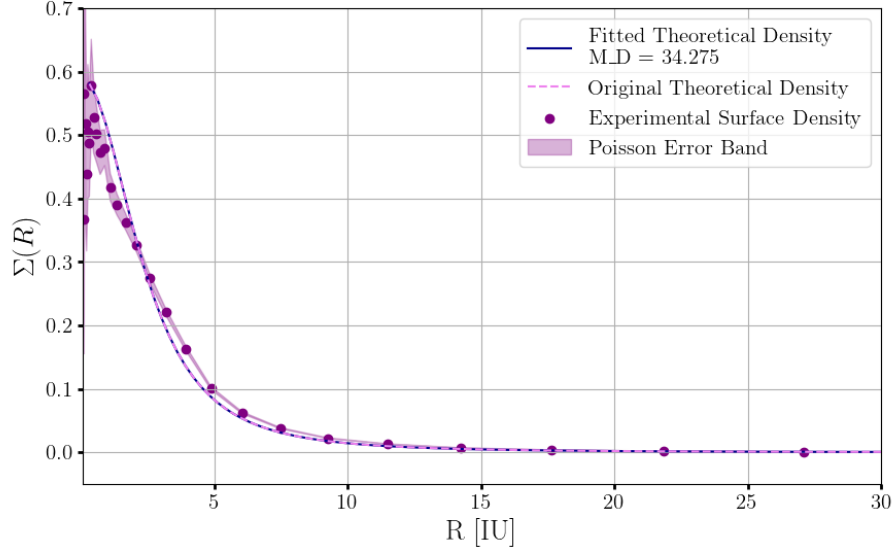
Figure 2: Surface density of a Miyamoto-Nagai disk as a function of R: comparison between the theoretical surface density (dashed pink line), the experimental surface density (purple dots with error bands), and the fitted surface density (solid blue line).

Once the cylindrical coordinates (R, θ, z) are determined, the corresponding cartesian coordinates (x, y, z) can be computed using the following equations:
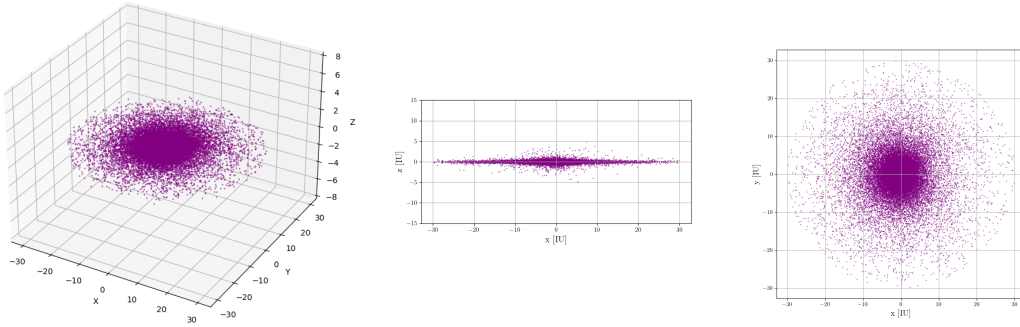
$$\begin{cases} x = R\cos(\theta) \\ y = R\sin(\theta) \\ z = z \end{cases}$$

Figure 3: Visualization of the 20000 particles in the Miyamoto-Nagai disk. The distribution is shown in 3D space (left), in the xz-plane (center), and in the xy-plane (right).

3.2   Disk Particles Velocities

In an axisymmetric potential, the symmetry around the z-axis implies that the potential, $\Phi(R, z)$, depends only on the cylindrical coordinates R and z, and is independent of the azimuthal angle θ. This symmetry results in the conservation of the z-component of angular momentum, L_z, which remains constant throughout the motion. Consequently, the motion of a particle is confined to a meridional plane, which is a plane defined by the rotation axis and the

particle's position. This reduces the complexity of the motion, making the dynamics separable into radial, azimuthal, and vertical components.

As shown in section 3.2 of [6], the equations of motion in axisymmetric potentials demonstrate that circular orbits are possible only in the equatorial plane ($z = 0$).

In disk galaxies, most particles follow quasi-circular orbits. This allows us to apply the epicyclic approximation, where the motion is treated as small oscillations around a circular orbit. These oscillations are developed by expanding the effective potential around $x = R - R_{\mathrm{guid}}$, where x is small. The guiding radius, R_{guid}, corresponds to the radius of a perfect circular orbit in the plane $z = 0$.

In our disk model the radial velocities (v_R) follow a Gaussian distribution centered at zero, consistent with the oscillatory nature of epicyclic motion. Consequently, the azimuthal velocities v_θ are centered around the circular velocities v_{circ}, which are expressed by the following equation:

$$v_{\mathrm{circ}}(R) = \sqrt{R \cdot \left.\frac{\partial \Phi_{\mathrm{tot}}}{\partial R}\right|_{z=0}} = \sqrt{R \cdot \left.\frac{\partial (\Phi_{\mathrm{disk}} + \Phi_{\mathrm{halo}})}{\partial R}\right|_{z=0}}. \tag{11}$$

The derivative of the potential, which accounts for both the disk and halo contributions, takes the form:

$$\left.\frac{\partial \Phi_{\mathrm{tot}}}{\partial R}\right|_{z=0} = \left.\frac{\partial (\Phi_{\mathrm{disk}} + \Phi_{\mathrm{halo}})}{\partial R}\right|_{z=0} = GR \left(M_D \left[(a_D + b)^2 + R^2 \right]^{-\frac{3}{2}} + M_H (R + a_H)^{-2} R^{-1} \right) \tag{12}$$

Regarding vertical equilibrium we consider an isothermal sheet approximation since the ratio between vertical and radial scales is much less than 1 ($b/a_D = 0.05$)

$$f(v_z | z) = \frac{1}{\sqrt{2\pi}\sigma_z} \exp\left(-\frac{v_z^2}{2\sigma_z^2} \right). \tag{13}$$

In this framework the velocity dispersion σ_z is related to the vertical scale parameter of the disk b as follows: [2]

$$\sigma_z = b\pi G\Sigma(R), \tag{14}$$

where the surface density Σ_R is expressed in equation 8.

For simplicity and under the assumption of isotropy, we set $\sigma_R = \sigma_\theta = \sigma_z(R)$ and so to ensure the disk's structural integrity, we used the Toomre stability criterion [9]. This criterion quantifies the balance between gravitational self-attraction and velocity dispersion, requiring $Q > 1$. We verified this condition in our case for every particle, using the inverse of the following equation:

$$\sigma_R(R, Q) = \frac{3.36 \cdot Q \cdot G \cdot \Sigma(R)}{\kappa}, \tag{15}$$

in which κ is the epyciclic frequency and it can be computed via

---

[2]Check [7] and section 11.4.2 of [8] for further details about it.

$$\kappa(R) = \sqrt{\left.\frac{\partial^2 \Phi_{\text{eff}}}{\partial R^2}\right|_{z=0, R=R_{\text{guid}}}}$$

$$= \sqrt{\left.\frac{\partial}{\partial R}\left(\frac{\partial}{\partial R}\left(\Phi_{\text{tot}} + \frac{1}{2}\frac{L_z^2}{R^2}\right)\right)\right|_{z=0, R=R_{\text{guid}}}}$$

$$= \sqrt{\left.\frac{\partial}{\partial R}\left(\frac{\partial \Phi_{\text{tot}}}{\partial R} - \frac{L_z^2}{R^3}\right)\right|_{z=0, R=R_{\text{guid}}}}$$

$$= \sqrt{\left.\frac{\partial^2 \Phi_{\text{tot}}}{\partial R^2} + \frac{3L_z^2}{R^4}\right|_{z=0, R=R_{\text{guid}}}}$$

$$= \sqrt{\left.\frac{\partial^2 \Phi_{\text{tot}}}{\partial R^2} + 3\Omega^2\right|_{z=0, R=R_{\text{guid}}}}$$

$$= \sqrt{\left.\frac{\partial^2 \Phi_{\text{tot}}}{\partial R^2} + \frac{3}{R}\frac{\partial \Phi_{\text{tot}}}{\partial R}\right|_{z=0, R=R_{\text{guid}}}}. \tag{16}$$

Below you can find the computation of the second derivative of the potential,

$$\left.\frac{\partial^2 \Phi_{\text{tot}}}{\partial R^2}\right|_{z=0} = \frac{1}{R}\frac{\partial \Phi_{\text{tot}}}{\partial R} + GR\left[M_D \cdot \left(-3R \cdot \left((a+b)^2 + R^2\right)^{-\frac{5}{2}}\right)\right] + $$
$$- GR\left[M_H \cdot \left(2 \cdot (R+a_H)^{-3} \cdot R^{-1} + (R+a_H)^{-2} \cdot R^{-2}\right)\right]. \tag{17}$$

The following summarizes the velocity distributions used in our model:

$$\begin{cases} v_R = \sigma_z \cdot \mathcal{N}(0,1), \\ v_\theta = v_{\text{circ}}(R) + \sigma_z \cdot \mathcal{N}(0,1), \\ v_z = \sigma_z \cdot \mathcal{N}(0,1), \\ v_x = -v_\theta \cdot \sin(\theta) + v_R \cdot \cos(\theta), \\ v_y = v_\theta \cdot \cos(\theta) + v_R \cdot \sin(\theta). \end{cases}$$
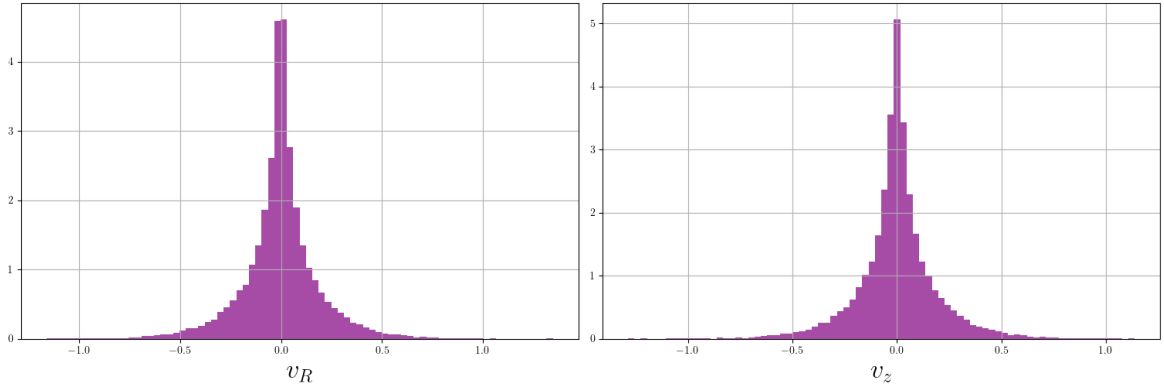

Figure 4: Distributions of the sampled velocities of the particles in a Miyamoto-Nagai disk embedded in a static Hernquist halo, shown fot the R direction (left) and the z directions (right).
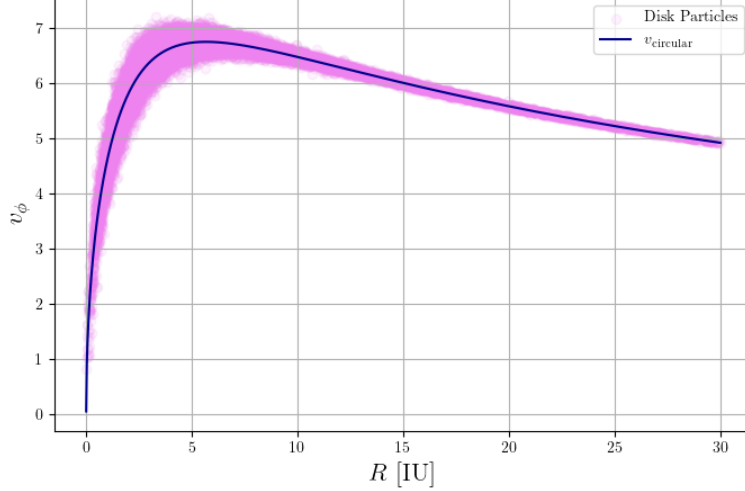
Figure 5: Sampled velocities of the particles in a Miyamoto-Nagai disk embedded in a static Hernquist halo in the ϕ direction as a function of R, compared with the circular velocity (blue line).

3.3 Perturber Initialization

The analysis was conducted using three different perturber masses to investigate the system's response to varying perturbations. The first case considers a perturber mass 500 times that of a single disk particle: $M_P = 0.857\,\mathrm{IU} \simeq 0.025\,M_D$. The other two simulations were done with half mass ($M_{\mathrm{half}} = 0.428\,\mathrm{IU}$) and double mass ($M_{\mathrm{double}} = 1.714\,\mathrm{IU}$) of the primary perturber. In all three scenarios, the mass hierarchy $m_{\mathrm{particle}} \ll M_P \ll M_D$ is maintained, with $m_{\mathrm{particle}} = 0.0017\,\mathrm{IU}$ and $MD = 34.28\,\mathrm{IU}$. This condition ensures that while the perturber is massive enough to influence nearby particles, it remains sufficiently small compared to the disk mass to cause only local symmetry breaking in the particle distribution. For each perturber mass configuration, the initial potition remains the same: the angular coordinate is set to $\theta_P = \pi/3$, while the radial distance is chosen to be less than twice the scale radius of the disk, $R_P = 5.2$. The vertical position is determined as the mean z-coordinate of all disk particles for simplicity: $z = -0.0026\mathrm{IU}$. The circular velocity of the perturber is computed using Equation 11, from which its x and y velocity components are computed. The z velocity component is sampled in the same way as for the disk particles, as described earlier.

3.4 Treecode parameters

In order to run the simulation, two parameters needed to be tuned: the softening parameter ε and the time step δt.

The softening parameter has a role in mitigating the effect of interactions between particles when their separation is close to zero. To estimate it we computed an approximate volume of the system by considering the total mass and dividing it by the maximum value of its density. Then, we divided this volume by the number of particles to estimate the volume occupied by a single particle. Finally, we took the cube root of this value to obtain a length scale.

$$\varepsilon = \left(\frac{V}{N}\right)^{1/3} = \left(\frac{M}{\max(\rho_D)}\frac{1}{N}\right)^{1/3} \tag{18}$$

In relation to this, we have tuned the time step, which controls when the code computes the accelerations. To maintain numerical stability and to ensure that the system is correctly described

we computed the time step taking a fraction of the square root of the ratio between the softening parameter (which represents the minimum length scale) and the maximum acceleration that the particles can experience. To compute the total acceleration, we sum the accelerations due to the Hernquist halo and the Miyamoto-Nagai potential in the radial direction ($a = -\nabla\Phi$).

$$\delta t = 0.5\sqrt{\frac{\varepsilon}{\max(a)}}. \tag{19}$$

For all the simulations we let the system to evolve for $12T_{\mathrm{dyn}}$, estimating the dynamical timescale with the following approximation

$$T_{\mathrm{dyn}} = \sqrt{1/<\rho_D>}, \tag{20}$$

in our case the dynamical timescale was $T_{\mathrm{dyn}} = 1.88[IU]$

Parameter	Numerical Value [IU]
ε	0.096
δt	0.0007
T_{stop}	22.8
θ	0.2

Table 1: Parameters used in the simulation of a Miyamoto-Nagai disk embedded in a static Hernquist halo.

For the perturbed simulations all the parameters were recalculated, with adjustments made only to δt and ε at the fourth and third decimal places, respectively. To perform our simulations, the main function of the treecode was modified to include the static spherical Hernquist potential which acts on the particles.

4 Results and Analysis

4.1 Equilibrium Analysis of the Disk-Halo System

The analysis of equilibrium begins with visualizing the motion of the center of mass (COM) relative to the origin. Below, the 3D radius is plotted as a function of time:
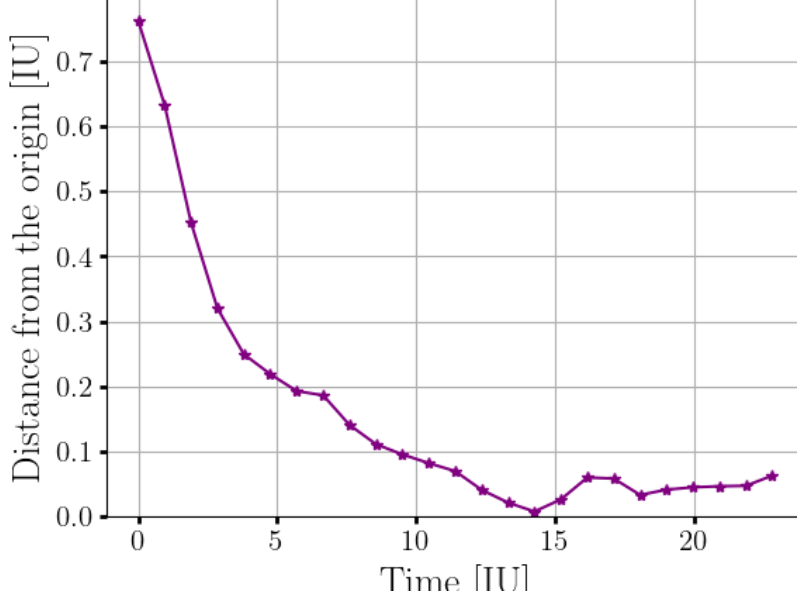
Figure 6: Time evolution of the center-of-mass distance from the origin for a Miyamoto-Nagai disk embedded in a static Hernquist halo.

The COM shifts over time, likely due to the finite number of particles in the system. All subsequent computations will be performed in the COM frame of reference (FoR).

To analyze the equilibrium state we computed and plotted the Lagrangian radii over time. They are defined as the radial distances within which a specific percentage of the system's total mass is enclosed.
To quantify deviations from equilibrium, we computed the residuals of the Lagrangian radii relative to their initial values.
Looking at these two plots (7), (8), we can safely say that the system is at equilibrium for all the 12 dynamical timescales, with the residuals that never exceed the 4%.
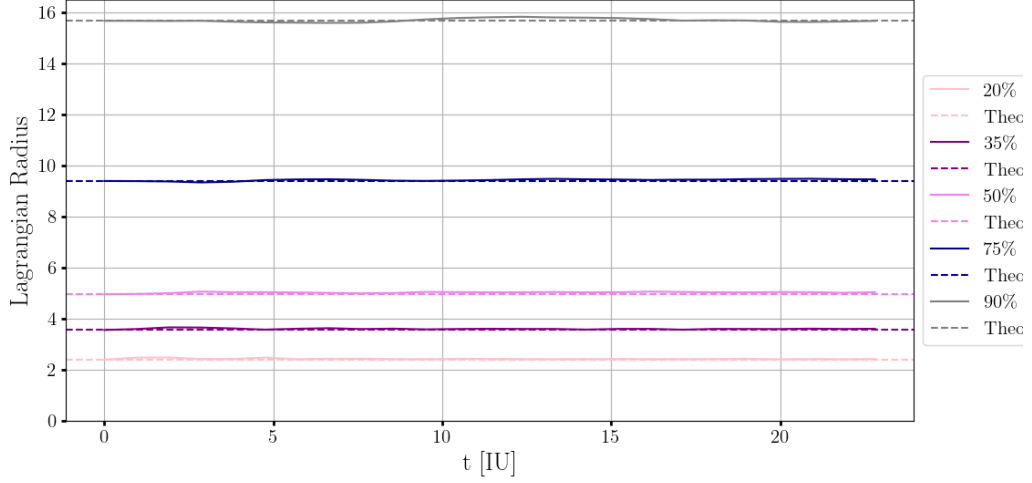
Figure 7: Time evolution of the Lagrangian radii of a Miyamoto-Nagai disk embedded in a static Hernquist halo, with the theoretical initial values indicated.
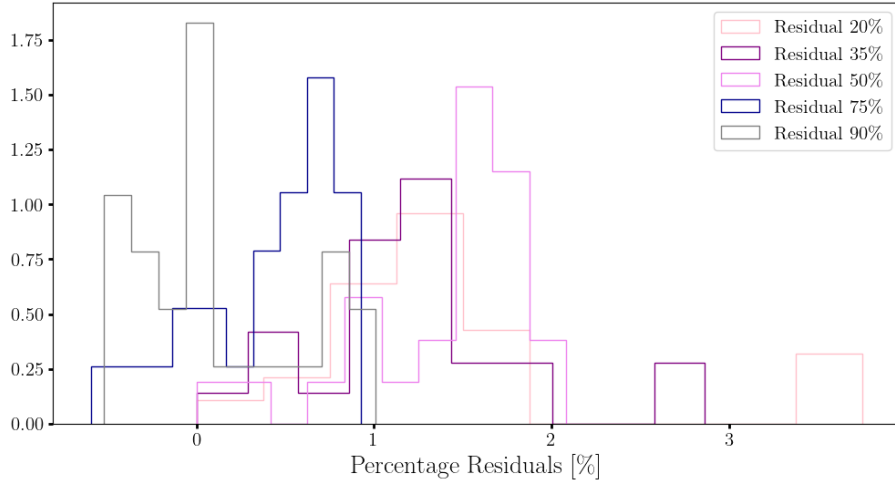
Figure 8: Histograms of the percentage residuals of the Lagrangian radii, calculated from the values shown in Figure 7, highlighting deviations from the theoretical initial values.

To further investigate the equilibrium state, we analyzed the evolution of the system's surface density 8 over time. The surface density analysis, presented in figure (9), aligns with the findings from the Lagrangian radii, confirming that the system remains in equilibrium within the limits of the Poisson errors associated with the numerical surface density.

The calculation used to generate these plots follow the same procedure introduced in section 3.1.
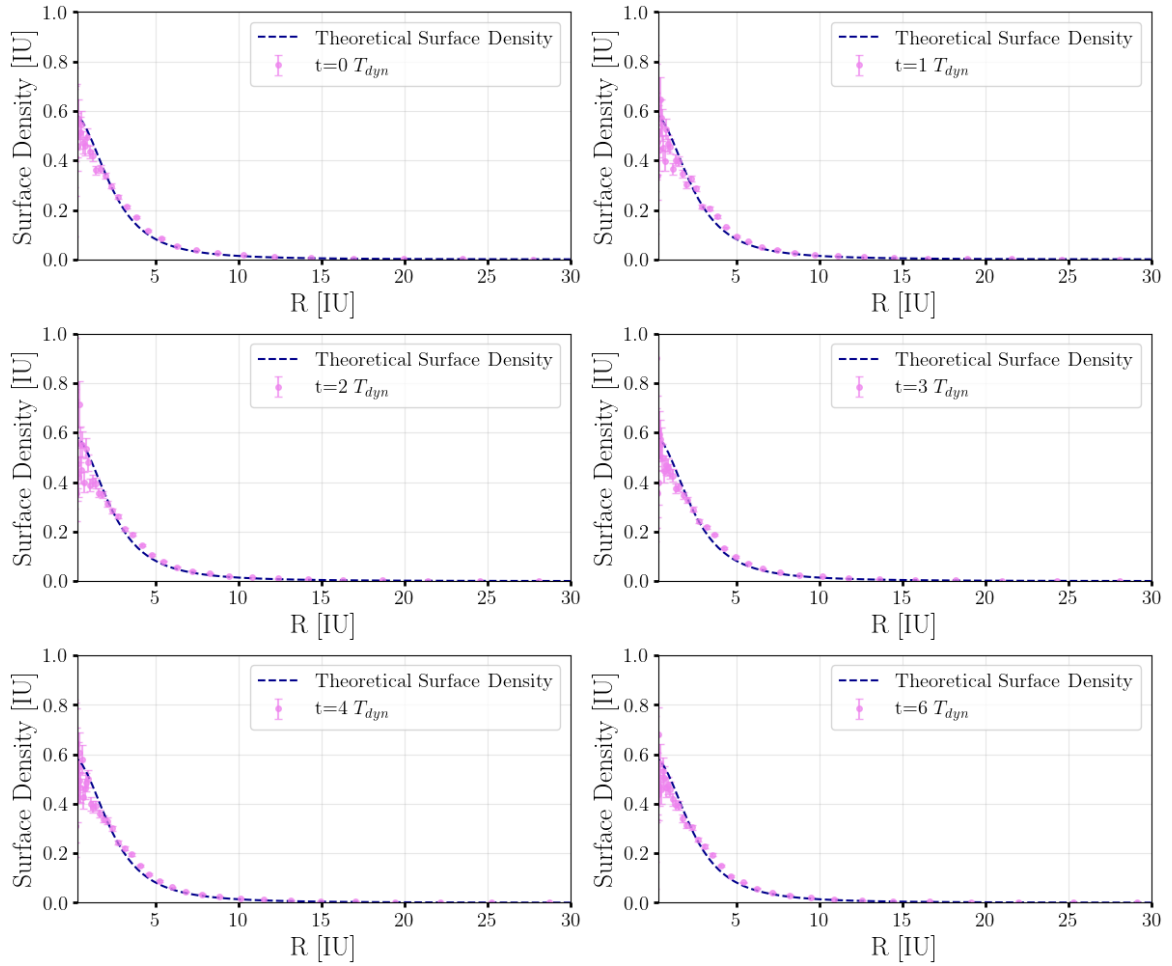
Figure 9: Comparison between the numerical surface density of the Miyamoto-Nagai disk embedded in a static Hernquist halo and the theoretical profile at different time instants. The theoretical profile is shown as a dashed blue line, while the numerical profile includes Poissonian error bars.

To check if any particles are escaping the system, we can plot the 3D velocities of disk's particles as a function of the 3D radius r at different time instants. By comparing these velocities to the escape velocity, we found that only one particle escapes the system.
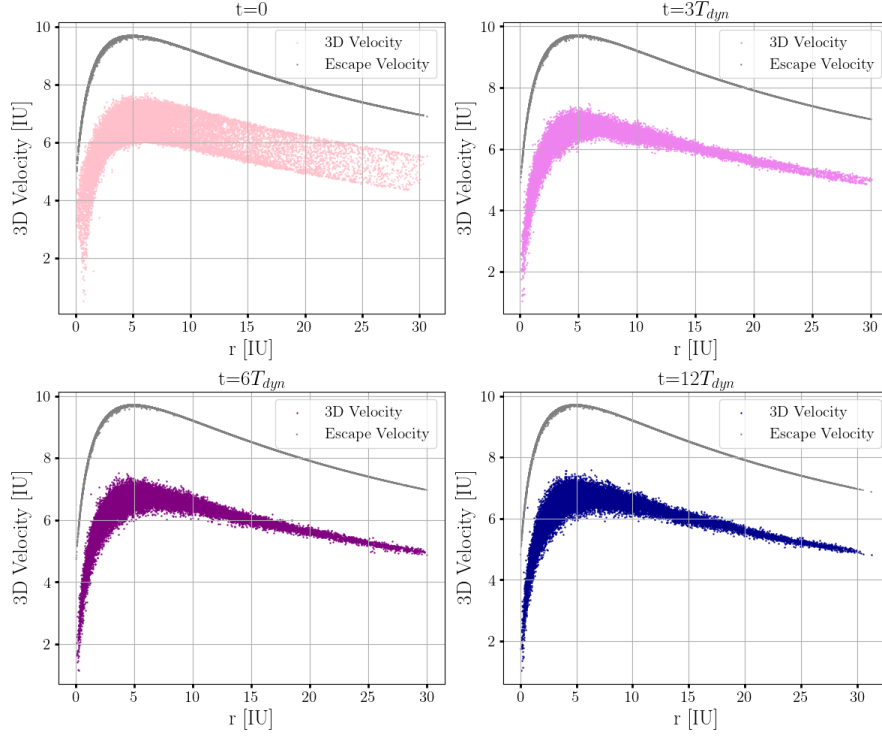
Figure 10: Comparison between the 3D velocities of the Myiamoto-Nagai disk particles (embedded in a static Hernquist halo) and the escape velocity (shown in grey) at different time instants.

4.1.1 Conserved Quantites

The last two aspects we analyzed to assess the system's equilibrium are the time evolution of energy and the time evolution of angular momentum in the z direction, both of which we expect to be conserved. We used the log file of the treecode to save the kinetic energy of the particles and the potential energy of the disk component of the system. Since the DM halo is necessary for maintaining the system's equilibrium, we manually added this term using the analytic potential from equation 5. The total energy is: Total Energy = $T+U_{disk}+U_{halo}$.
As shown in Figure 11, the energy is conserved, with fluctuations of the residuals around zero that never exceed 1%.
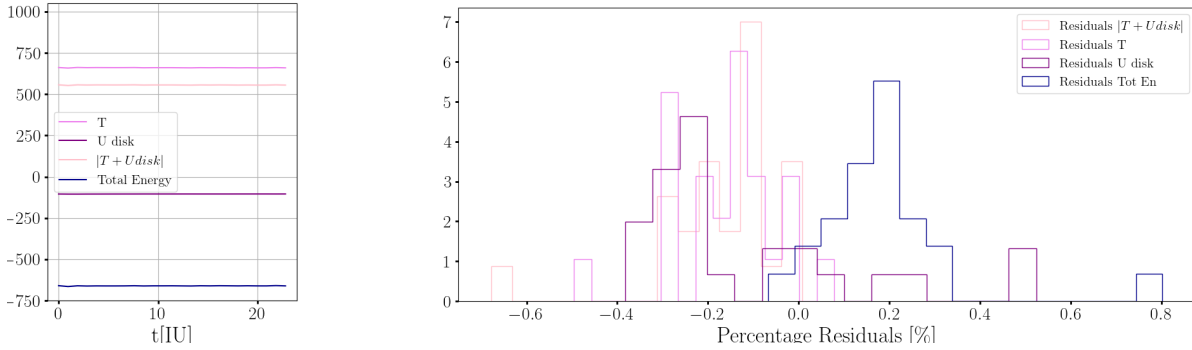
Figure 11: Left: plot of the energies over time of a Myiamoto-Nagai system embedded in a static Hernquist halo. Right: histograms of the percetage residuals of the energies in the left plot.

In the plot in Figure 12 is shown the time evolution of the z component of the total angular

momentum of the system in the COM FoR. We can see that after three timesteps (one dynamical time), during which the system's angular momentum increases by 1.29%, the angular momentum remains essentially constant.
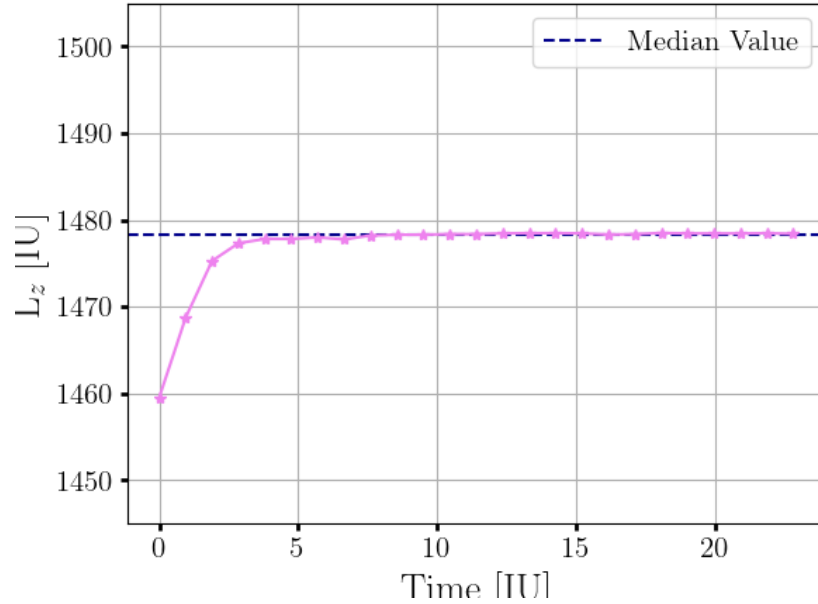

Figure 12: Evolution over time of the z-component of the total angular momentum of a Myiamoto-Nagai system embedded in a static Hernquist halo. The dashed blue line represents the median value of it.

4.2 Analysis of the perturbed system

To analyze the behavior of the perturbed system, the three simulations initialized as described in Section 3.3 were conducted with the goal of investigating the effect of dynamical friction and how it depends on the perturber's mass.

At this link you can find a GIF that shows the evolution of our perturbed system over time with the initial perturber of mass $M_P = 0.857\,\mathrm{IU}$.

The first set of results focuses on the motion of the system's center of mass for each of the three cases. Figure 13 illustrates the COM motion for the three perturbers. We can clearly observe that the COM shows more fluctuations in the presence of a more massive perturber. This could be caused by the fact that a more massive perturber induces greater instabilities in the system, leading to a higher movement of the particles.
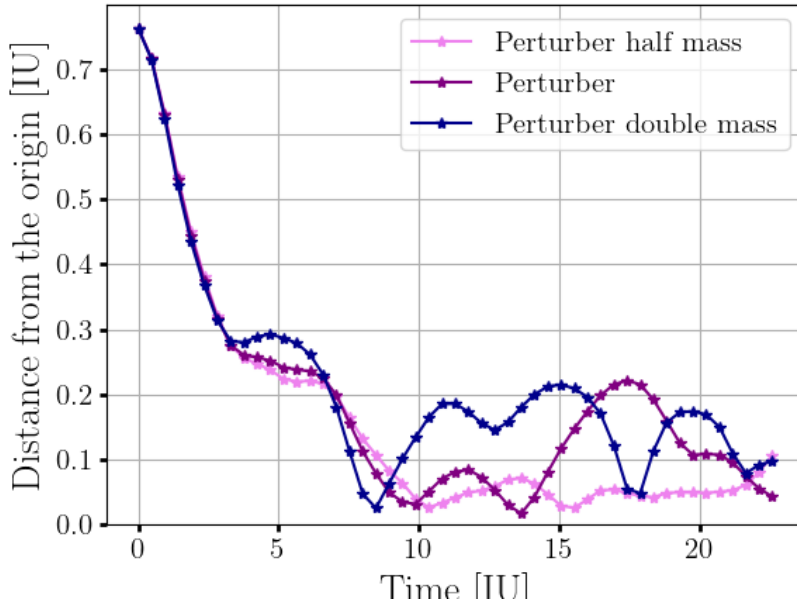
Figure 13: 3D radial motion of the center of mass of a Miyamoto-Nagai disk system embedded in a static Hernquist halo, perturbed by three different masses over time.

From this point forward, all calculations are done in the COM frame of reference to ensure consistency. Next, the radial motion of the perturbers is compared across the three simulations. Figure 14 displays the trajectories over time. Two key observations can be made. First, the effect of dynamical friction on the less massive perturber appears much later compared to the other two cases. In particular its motion remains regular until $t \sim 10\,\mathrm{IU}$, while the motions of the other two perturbers start to be deflected around $t \sim 6\,\mathrm{IU}$. Second, as expected, the more massive perturber travels closer to the COM more rapidly, consistent with the stronger dynamical friction acting on it.
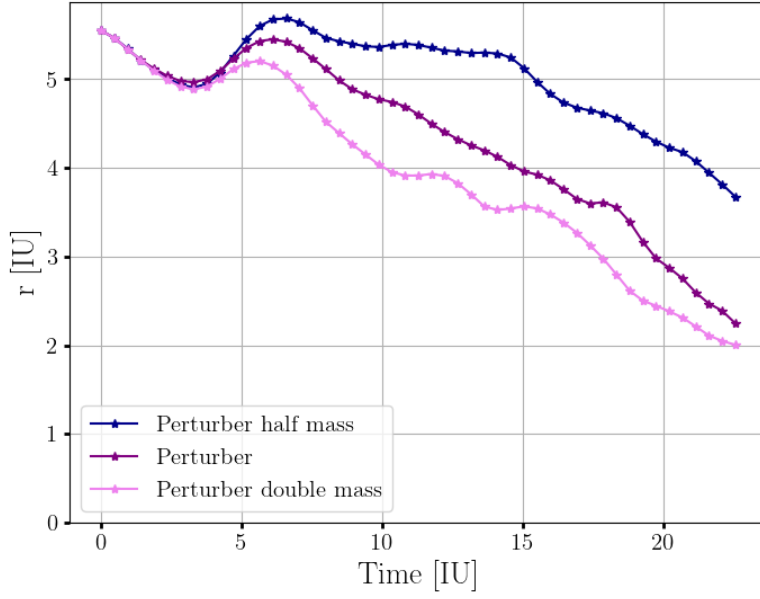
Figure 14: 3D radial motion in the CoM FoR of three perturbers in a Miyamoto-Nagai disk system embedded in a static Hernquist halo as a function of time.

We now plot the radial velocity of the perturber, confirming that it decreases over time (Figure 15). The same trend as before is observed: the initial perturber slows down by 16.6%, the more massive one by 19.5%, while the less massive perturber slows down by only 8%.
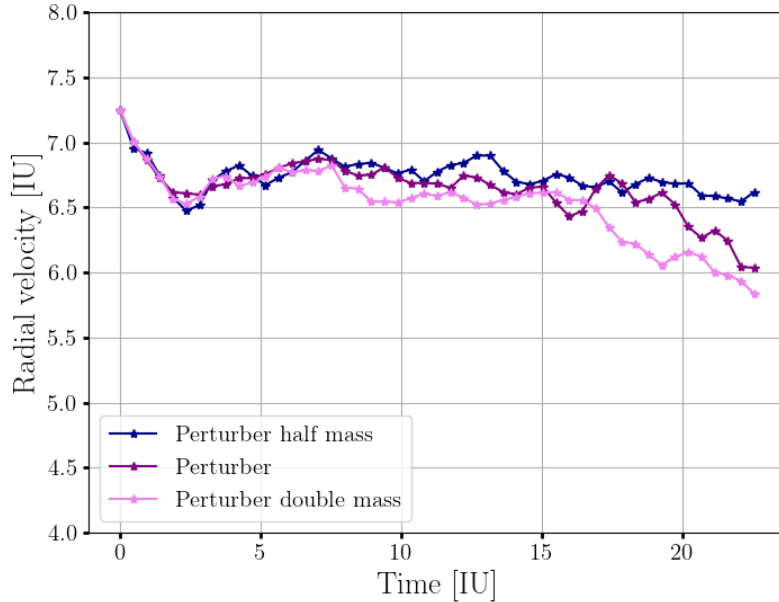

Figure 15: 3D radial velocities in the CoM FoR of three perturbers in a Miyamoto-Nagai disk system embedded in a static Hernquist halo as a function of time.

The fact that the radial velocity of the perturber decreases suggests, as expected, that it is exchanging kinetic energy with the particles of the disk, whose velocities should increase in the regions near the perturber. This phenomenon is illustrated in Figures 16, 17, 18.
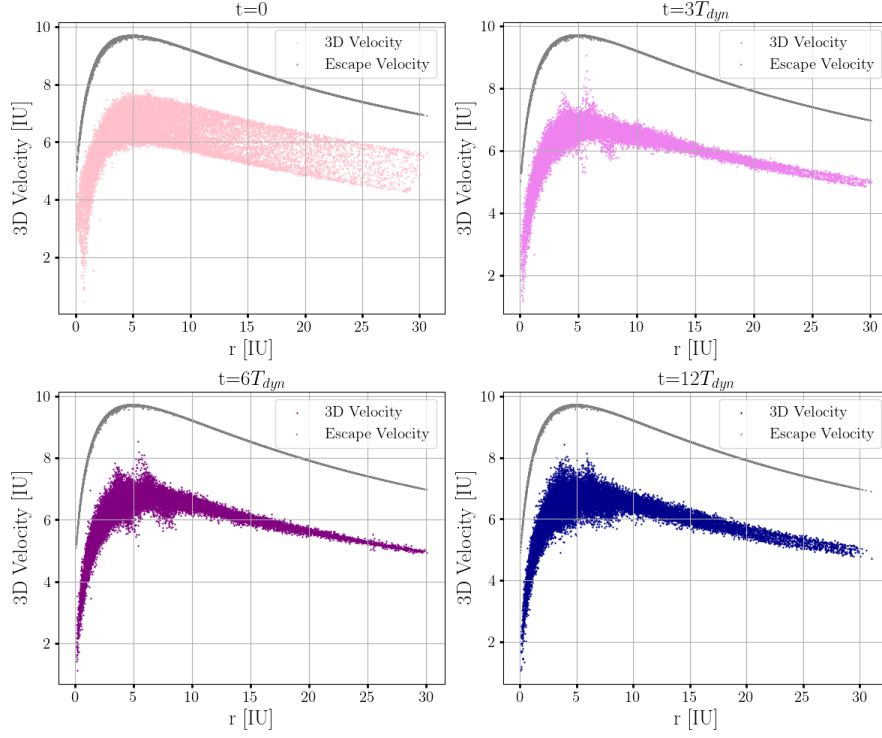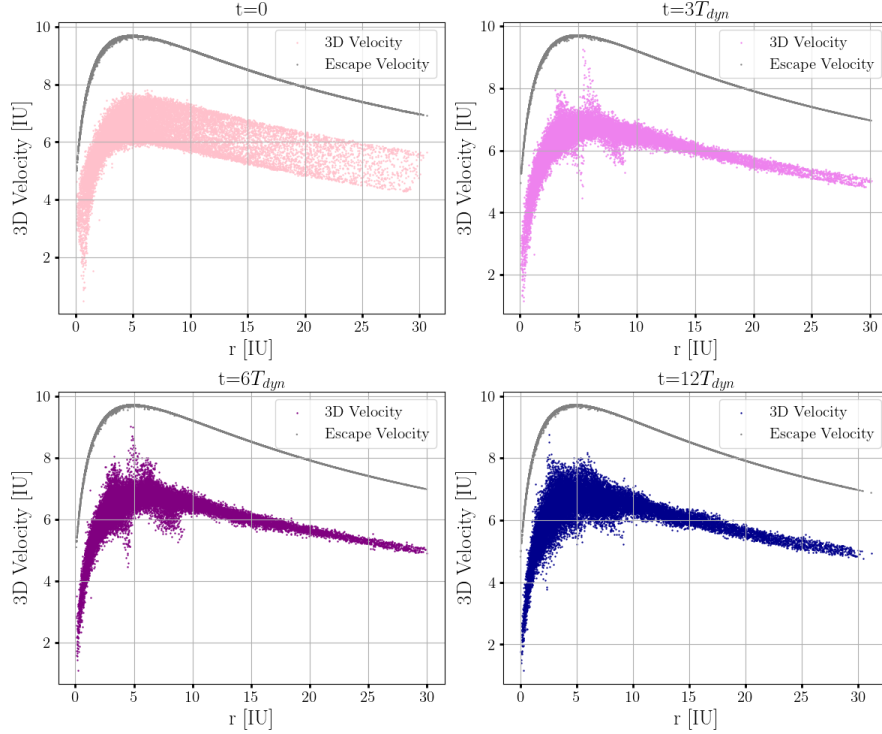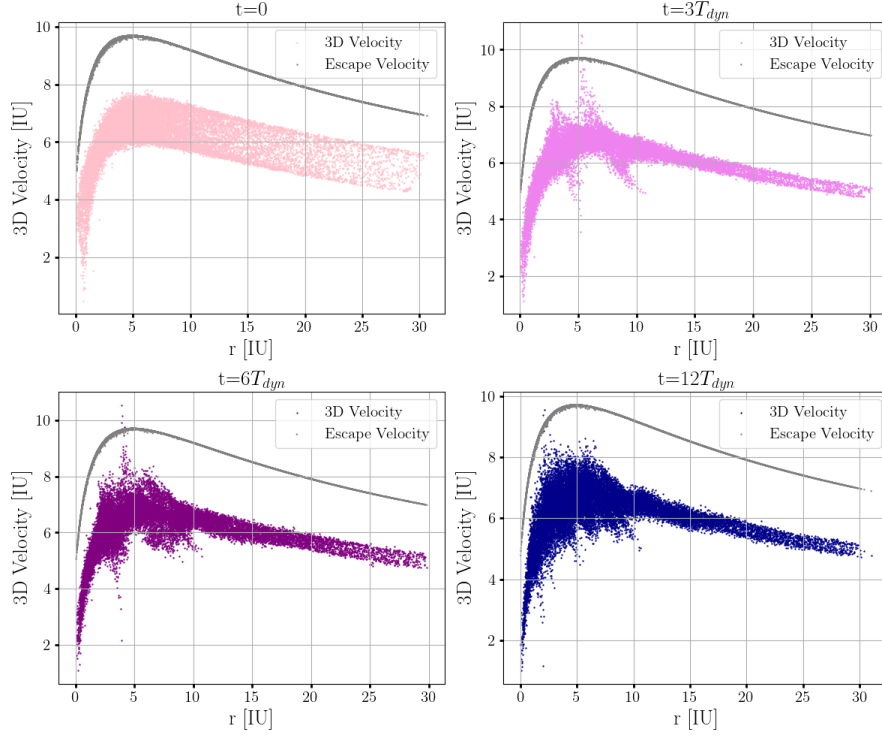
Figure 16: Comparison between the 3D velocities of the Miyamoto-Nagai disk particles (embedded in a static Hernquist halo) and the escape velocity (shown in grey) at different time instants. The system is perturbed by a light perturber with a mass of $M_{half} = 0.428\,IU$.

Figure 17: Comparison between the 3D velocities of the Miyamoto-Nagai disk particles (embedded in a static Hernquist halo) and the escape velocity (shown in grey) at different time instants. The system is perturbed by a perturber with a mass of $M_P = 0.857\,IU$.

Figure 18: Comparison between the 3D velocities of the Miyamoto-Nagai disk particles (embedded in a static Hernquist halo) and the escape velocity (shown in grey) at different time instants. The system is perturbed by a massive perturber with a mass of $M_{double} = 1.714\,IU$

The number of particles whose velocity exceeds the escape velocity is very small: a maximum of 3 for the initial perturber, a maximum of 1 for the less massive perturber, and a maximum of 15 for the more massive one. Since these are all negligible numbers compared to the total amount of particles (20000), the total energy of the system should be conserved. I verified this condition in all three cases, and the results are shown in Figures 19, 20, and 21.
As in the equilibrium case the residuals of the total energy never exceed 1%.
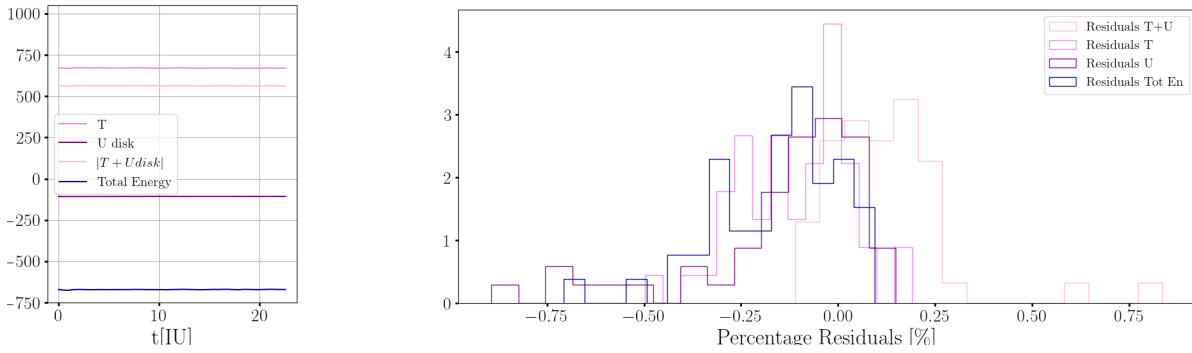
Figure 19: Left: plot of the energies over time of a Myiamoto-Nagai disk embedded in a static Hernquist halo, perturbed by a mass of $M_{half} = 0.428\,IU$. Right: histograms of the percetage residuals of the energies in the left plot.

18

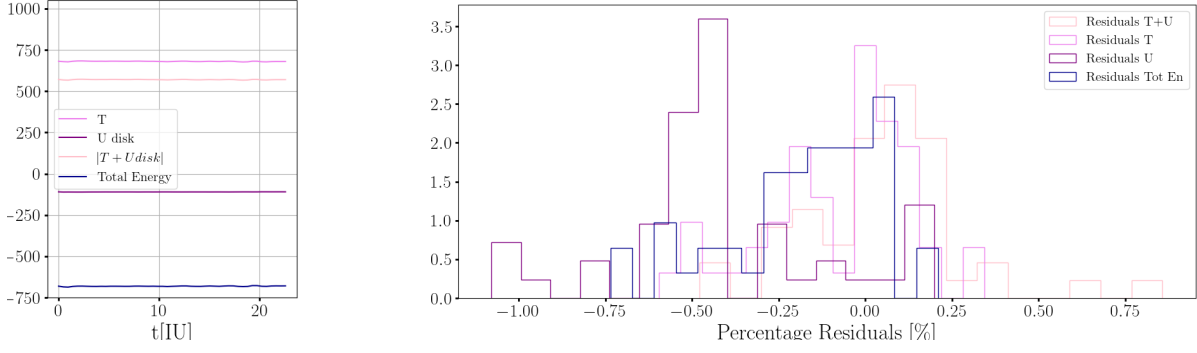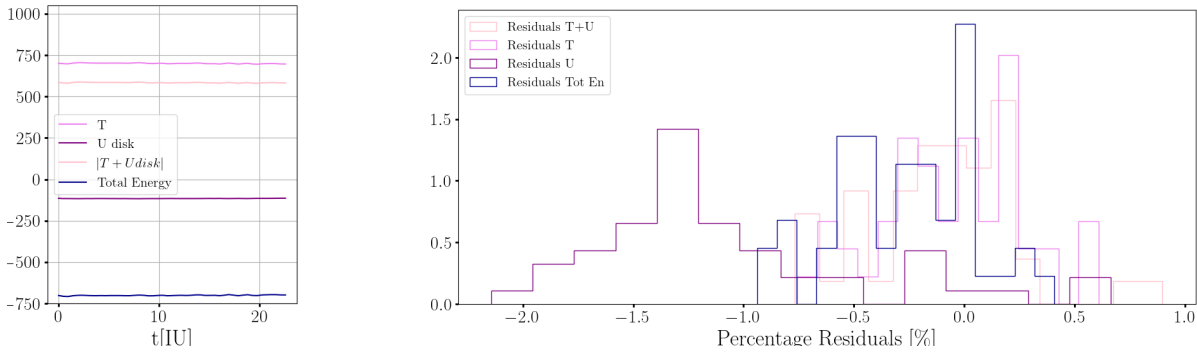Figure 20: Left: plot of the energies over time of a Myiamoto-Nagai disk embedded in a static Hernquist halo, perturbed by a mass of $M_P = 0.857\,\mathrm{IU}$. Right: histograms of the percentage residuals of the energies in the left plot.

Figure 21: Left: plot of the energies over time of a Myiamoto-Nagai disk embedded in a static Hernquist halo, perturbed by a mass of $M_{double} = 1.714\,\mathrm{IU}$. Right: histograms of the percentage residuals of the energies in the left plot.

With the introduction of a perturber the axial symmetry of the original system is broken and without it there is no physical reason to expect the conservation of L_z. Plotting the time evolution of the total L_z of the disk particles (Fig. 22), we notice that the magnitude increase scales with the perturber's mass, as expected from the stronger gravitational torques and more significant symmetry breaking induced by a more massive perturber. Then in Figure 23 is plotted the evolution of the angular momentum of the perturbers (only z-component is shown because x and y components are just fluctuations around zero).
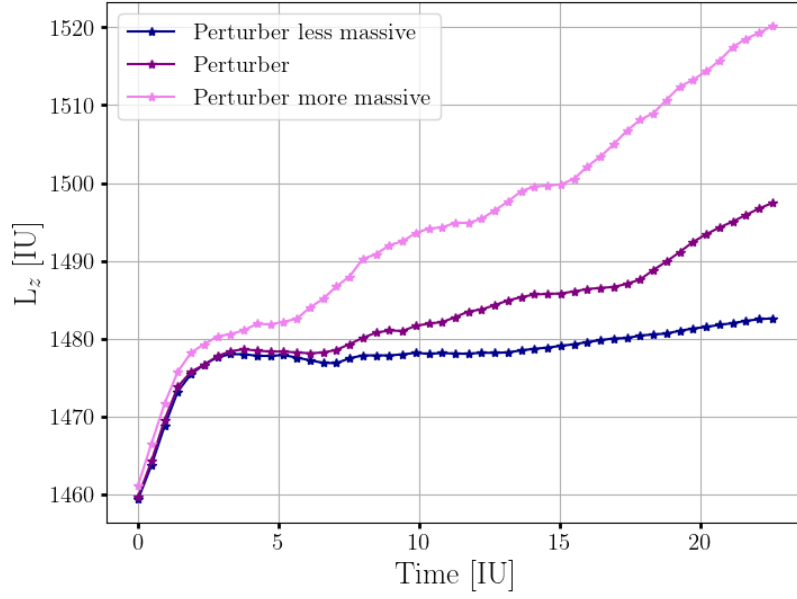
Figure 22: Time evolution of the z component of the total angular momentum of a Miyamoto-Nagai disk embedded in a Hernquist Halo in the COM FoR. The system is perturbed by three different masses.
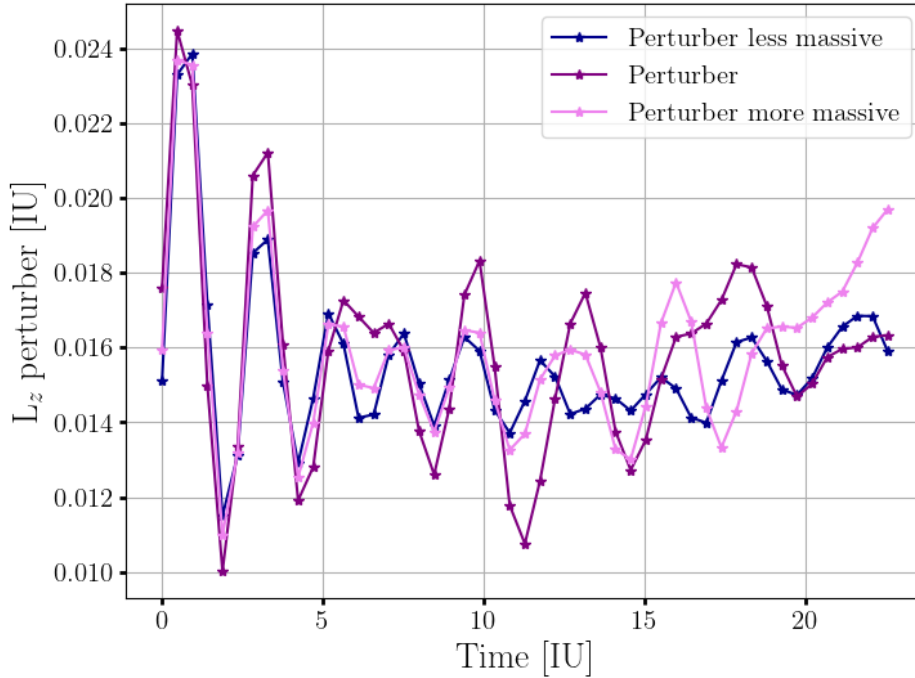

Figure 23: Time evolution of the z component of the angular momentum of the three different perturbers in a Miyamoto-Nagai disk embedded a Hernquist Halo, analyzed in the COM FoR.

In conclusion, we can also analyze the effect of the perturbers on the Lagrangian radii in the three cases (Figures 24, 26, 28). A deviation from the equilibrium state is observed in all cases, with a stronger effect for the more massive perturbers, where an expansion of the inner

Lagrangian radii is evident. The residuals reflect this behavior, reaching a deviation of up to 12% from zero.
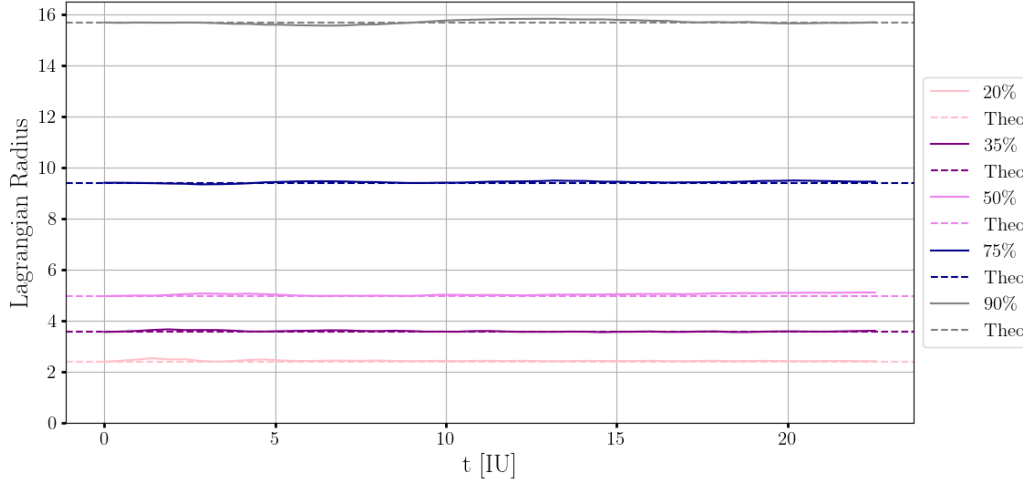

Figure 24: Time evolution of the Lagrangian radii of a Miyamoto-Nagai disk embedded in a static Hernquist halo, with the theoretical initial values indicated. The system is perturbed by a mass of $M_{half} = 0.428$, IU

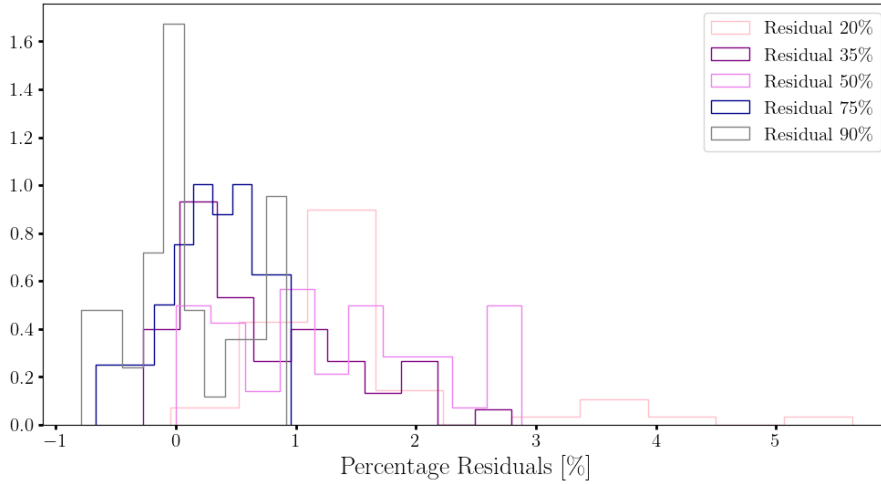Figure 25: Histograms of the percentage residuals of the Lagrangian radii, calculated from the values shown in Figure 24, highlighting deviations from the theoretical initial values.
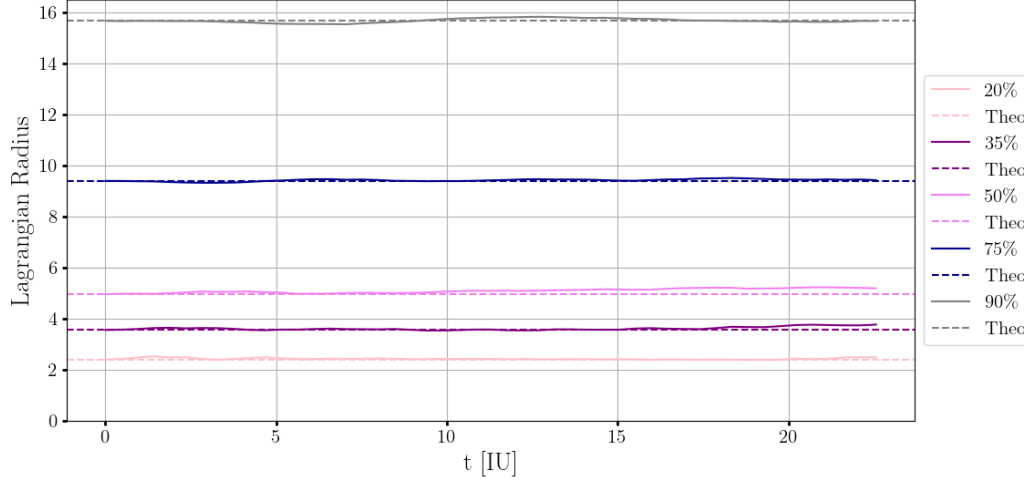
Figure 26: Time evolution of the Lagrangian radii of a Miyamoto-Nagai disk embedded in a static Hernquist halo, with the theoretical initial values indicated. The system is perturbed by a mass of $M_P = 0.857\,\mathrm{IU}$
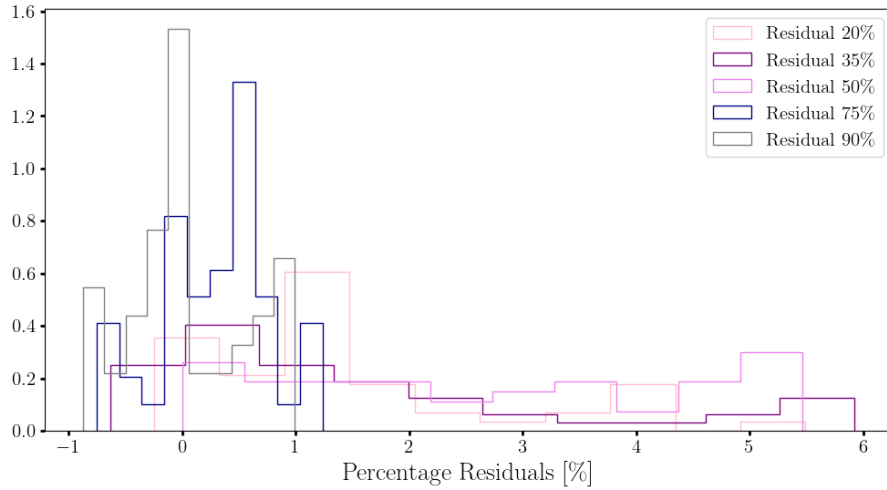

Figure 27: Histograms of the percentage residuals of the Lagrangian radii, calculated from the values shown in Figure 26, highlighting deviations from the theoretical initial values.
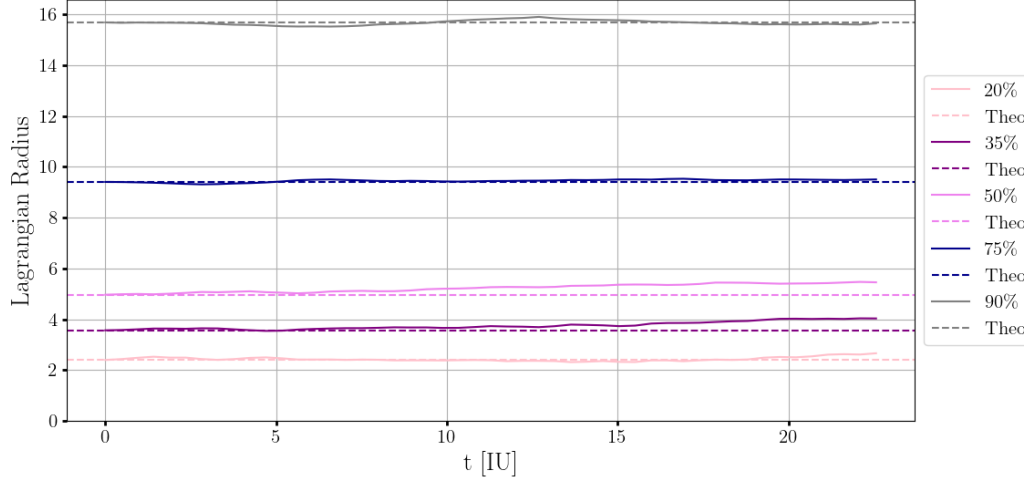
Figure 28: Time evolution of the Lagrangian radii of a Miyamoto-Nagai disk embedded in a static Hernquist halo, with the theoretical initial values indicated. The system is perturbed by a mass of $M_{double} = 1.714\,IU$
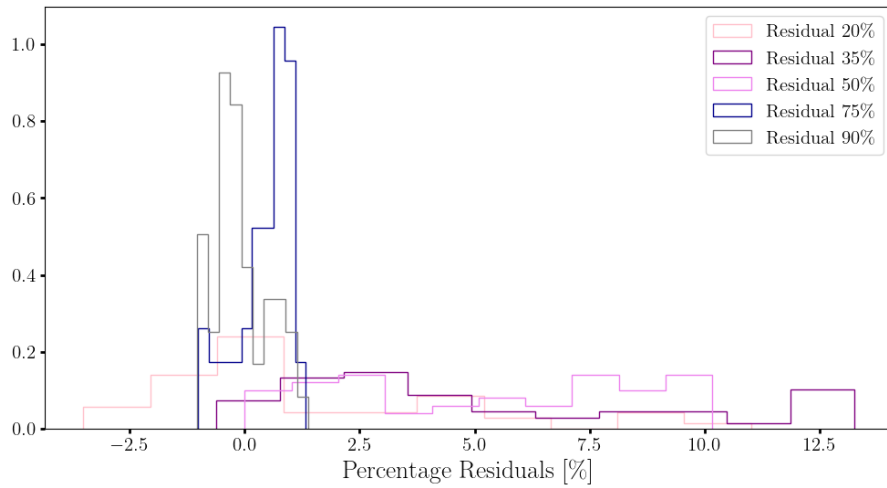

Figure 29: Histograms of the percentage residuals of the Lagrangian radii, calculated from the values shown in Figure 28, highlighting deviations from the theoretical initial values.

5 Conclusion

The system, consisting of a Miyamoto-Nagai disk embedded in a Hernquist halo, has been successfully initialized in equilibrium. This equilibrium is primarily confirmed by the conservation of energy and angular momentum, as well as the stability of the Lagrangian radii and the surface density distribution.

We then perturbed the system with a particle with mass $M_P = 0.857 \, \mathrm{IU}$ in one case, and with particles with double and half of this mass in the other two cases. It was observed that the more massive perturber transfers kinetic energy and angular momentum more efficiently to the system, leading to a faster orbital decay in a shorter timescale compared to the other two perturbers. This behavior is consistent with theoretical predictions from dynamical friction.

All the computations are collected in this git public repository.
The initialization of the system has been made with the collaboration of Malvina Bellotti, whom I thank.

References

[1] M. Miyamoto and R. Nagai. "Three-dimensional models for the distribution of mass in galaxies." In: 27 (Jan. 1975), pp. 533–543.

[2] H. C. Plummer. "On the Problem of Distribution in Globular Star Clusters: (Plate 8.)" In: *Monthly Notices of the Royal Astronomical Society* 71.5 (Mar. 1911), pp. 460–470. ISSN: 0035-8711. DOI: 10.1093/mnras/71.5.460. eprint: https://academic.oup.com/mnras/article-pdf/71/5/460/2937497/mnras71-0460.pdf. URL: https://doi.org/10.1093/mnras/71.5.460.

[3] Lars Hernquist. "An Analytical Model for Spherical Galaxies and Bulges". In: 356 (June 1990), p. 359. DOI: 10.1086/168845.

[4] Josh Barnes and Piet Hut. "A hierarchical O(N log N) force-calculation algorithm". In: 324.6096 (Dec. 1986), pp. 446–449. DOI: 10.1038/324446a0.

[5] Benjamin P. Moster, Rachel S. Somerville, Christian Maulbetsch, Frank C. van den Bosch, Andrea V. Macciò, Thorsten Naab, and Ludwig Oser. "CONSTRAINTS ON THE RELATIONSHIP BETWEEN STELLAR MASS AND HALO MASS AT LOW AND HIGH REDSHIFT". In: *The Astrophysical Journal* 710.2 (Jan. 2010), pp. 903–923. ISSN: 1538-4357. DOI: 10.1088/0004-637x/710/2/903. URL: http://dx.doi.org/10.1088/0004-637X/710/2/903.

[6] J. Binney and S. Tremaine. *Galactic Dynamics: Second Edition*. Princeton Series in Astrophysics. Princeton University Press, 2011. ISBN: 9781400828722. URL: https://books.google.it/books?id=6mF4CKxlbLsC.

[7] Piet van der Kruit. "Galactic Thin Disk". In: *Encyclopedia of Astronomy and Astrophysics* (Nov. 2000). DOI: 10.1888/0333750888/2863.

[8] Jo Bovy. *Dynamics and Astrophysics of Galaxies*. Princeton, NJ: Princeton University Press, 2022. ISBN: 978-0691235290. URL: https://press.princeton.edu/books/hardcover/9780691235290/dynamics-and-astrophysics-of-galaxies.

[9] A. Toomre. "On the gravitational stability of a disk of stars." In: 139 (May 1964), pp. 1217–1238. DOI: 10.1086/147861.